applied sciences

MDPI

Article

High-Temperature Open Volumetric Air Receiver Integrated with Compressed Air Energy Storage: Design of Experimental Prototype

Javier Baigorri [1,*], Xabier Rández [1], Rafael Pérez [2], Laura C. Alonso-Pardo [3], Antonio L. Ávila-Marín [3] and Fritz Zaversky [1]

[1] Department of Solar Energy Technologies & Storage, National Renewable Energy Centre (CENER), 31621 Sarriguren, Spain; xrandez@cener.com (X.R.); fzaversky@cener.com (F.Z.)
[2] Aalborg CSP A/S, Hjulmagervej 55, 9000 Aalborg, Denmark; rps@aalborgcsp.com
[3] CIEMAT-Plataforma Solar de Almería, 04200 Tabernas, Spain; laurac.alonso@ciemat.es (L.C.A.-P.); antonio.avila@ciemat.es (A.L.Á.-M.)
* Correspondence: jbaigorri@cener.com

Abstract

This study presents the design and modeling of a first-of-its-kind experimental prototype integrating a high-temperature air-based Concentrated Solar Power (CSP) receiver with a diabatic Compressed Air Energy Storage (CAES) system. The prototype architecture and operating modes are defined, and a detailed thermal model of an Open Volumetric Air Receiver (OVAR) is developed and optimized, with emphasis on passive mass flow regulation under non-uniform solar flux. At nominal conditions (800 °C), the receiver achieves a predicted thermal efficiency of 81.6%. Transient simulations assess off-design dynamic behavior under realistic conditions, showing sensitivity to solar fluctuations and need for heliostat aiming strategies to reduce thermal non-uniformities and ensure stable outlet temperatures. For the CAES subsystem, a techno-economic analysis identifies high-pressure (300 bar) commercial gas cylinders as the most cost-effective aboveground storage solution, while discharge simulations yield a required storage volume of 4.8 m^3. Finally, the complete piping and instrumentation diagram (P&ID) of the integrated system is presented, defining the experimental configuration. Overall, this work establishes the design basis for the future experimental demonstration of hybrid CAES-CSP operation for dispatchable renewable power generation and supports subsequent control development and scale-up analyses.

Keywords: concentrated solar power; compressed air energy storage; prototype; modeling; experimental approach; small-scale energy storage

Check for updates

Academic Editor: Maria Vicidomini

Received: 11 May 2026
Revised: 21 May 2026
Accepted: 3 June 2026
Published: 2 July 2026

1. Introduction

The rapid growth in global electricity consumption, driven by economic development and industrial activity, has heightened the urgency for sustainable power solutions. In response, there has been a pronounced shift toward renewable energy generation to reduce reliance on fossil fuels and lower greenhouse gas emissions [1]. However, large-scale deployment of variable renewable energy sources, such as wind and solar, introduces substantial operational challenges for electrical grids due to their intrinsic intermittency and the resulting temporal mismatch between energy supply and demand. Integrating

https://doi.org/10.3390/app16136633

energy storage systems has therefore emerged as a fundamental strategy for stabilizing power networks and enhancing renewable penetration [2].

Among the available energy storage technologies, Compressed Air Energy Storage (CAES) has received considerable research and development interest owing to its high operational reliability, long-duration storage capability, long service life, inherent provision of synchronous inertia, and overall economic viability [3,4]. CAES operates by using surplus electrical energy to compress air, which is then stored in high-pressure reservoirs during periods of low demand. When electricity demand increases, the stored compressed air is released, heated, expanded through turbines, and converted back into electrical energy.

CAES systems may be classified according to heat management strategy, storage mode, and scale, including diabatic (D-CAES), adiabatic (A-CAES), and isothermal configurations; isochoric or isobaric storage; and applications ranging from micro-CAES to utility-scale plants [5,6]. Among these options, D-CAES remains attractive for hybridization because external thermal input can be used to improve the expansion process and reduce fuel dependence. [7].

Furthermore, the integration of CAES with Concentrated Solar Power (CSP) has emerged as a promising option in regions with high solar resource availability, as CSP can provide supplementary thermal energy at the turbine inlet [8–12]. In the CSP sector, solar tower plants can also use air as heat transfer fluid, enabling operation at temperatures exceeding 800 °C, which leads to higher conversion efficiencies compared to conventional molten salt technologies, while also providing medium-temperature residual heat suitable for the decarbonization of industrial process heat. In this context, the present study is conducted within the framework of the Horizon Europe project "ASTERIx-CAESar" [13], which develops a pioneering hybrid concept that integrates a D-CAES configuration with solar-derived thermal input. The concept is based on an Open Volumetric Air Receiver (OVAR) coupled with packed-bed Thermal Energy Storage (TES), enabling the combined use of grid-stored electricity and dispatchable solar-driven electricity generation [14].

Open Volumetric Air Receiver technology has been widely studied through numerical modeling and design optimization, including open- and closed-loop configurations and ceramic or metallic absorber structures [15–17]. A key advantage of this concept lies in the volumetric absorption of solar radiation, which enhances heat transfer within the receiver and leads to higher thermal efficiencies compared to surface-based receiver designs [18]. As in other high-temperature solar receivers, receiver efficiency is strongly dependent on the operating temperature, since higher outlet temperatures increase thermal losses. However, despite its potential for high thermal efficiency, experimental validation remains limited to a small number of pilot or pre-demonstration projects, as summarized in Table 1 [19–21].

Table 1. Most relevant OVAR projects and expected specifications of the proposed prototype [15,22].

Name	Year	Material	Outlet Air Temperature (°C)	Thermal Efficiency, η_{rec} (%)	Power (kW_{th})	OVAR Type
SIREC	2001	Alloy 230	710	48 (experimental)	250	Wiremesh
SOLAIR 3000	2003	re-SiC	750	75 (experimental)	3000	Honeycomb
REFOS	1998–2009	Inconel 600	800	67 (experimental)	350	Wiremesh
CAPTure	2019	SiC	700	83 (theoretical)	300	Foam
CAES-CSP prototype	2026	SiSiC	800	>80	500	Foam

Similarly, the optimal design of the CAES system still presents challenges because storage pressure, turbomachinery performance, heat management, and operating strategy are strongly coupled. Therefore, several challenges remain from bringing CAES from theory to practice [23]. Future developments are expected to focus on the design of compact storage tanks with enhanced pressure tolerance, as well as compressors and expanders capable of operating at high pressure ratios and high efficiency [6,24]. Even then, there are some CAES facilities and projects worldwide, including micro-scale (<1 MW_e), small-scale (1–10 MW_e) and large-scale (10–500 MW_e) (see Table 2).

Table 2. State-of-the-art of CAES projects and expected specifications of the proposed prototype [25–35].

Scale	Name	Location	CAES Technology	Power Capacity	Volume (m^3)	Reservoir Type	Status
Large-scale	Huntorf	Germany	D-CAES	290 MW_e	310,000	Underground salt cavern	Operational
	McIntosh	USA	D-CAES	110 MW_e	570,000	Underground salt cavern	Operational/recently refurbished
	Jintan (Jiangsu) Phase 1	China	A-CAES	60 MW_e	220,000	Underground salt cavern	Operational
	Jintan (Jiangsu) Phase 2	China	A-CAES	2 × 350 MW_e	1,200,000	Underground salt cavern	Announced
	Zhangjiakou	China	A-CAES	100 MW_e	—	Steel tanks	Uncertain
	Silver City	Australia	A-CAES	200 MW_e	250,000	Aboveground hard rock	Approved
Small-scale	Goderich	Canada	A-CAES	1.75 MW_e	10,000	Repurposed salt cavern	Operational
	ALACAES	Switzerland	A-CAES	1 MW_e	2500	Unused mountain tunnel	Testing/design complete
	RICAS2020	Austria	A-CAES	5 MW_e	2000	Unused mountain tunnel	Testing/design complete
	Langfang	China	A-CAES	1.5 MW_e	760	Steel tanks	Uncertain
Micro-scale	UFMG	Brazil	A-CAES	9 kW_e	5	—	Testing/design complete
	IMT Atlantique	France	T-CAES	2 kW_e	0.3	Gas cylinders	Testing/design complete
	UET Peshawar	Pakistan	A-CAES	0.6 kW_e	0.5	Steel tank	Testing/design complete
	Montreal	Canada	A-CAES	62 kW_e	6	Gas cylinders	Charging testing/pending integration of turbines
	Beijing	China	A-CAES	430 kW_e	100	Steel tanks	Testing/design complete
	CAES-CSP prototype	Spain	D-CAES	50 kW_e	5	Gas cylinders	Under construction

Although numerous studies have analyzed CSP and CAES from a theoretical standpoint and proposed various system optimizations, experimental validation remains scarce. In particular, no prototype has yet integrated both technologies into a single system. This paper addresses that gap by presenting the design of a first-of-its-kind prototype that couples air-based high-temperature CSP with CAES. The study provides a comprehensive guide to the modeling, calculations, and design decisions underlying the development of the prototype, providing a dynamic simulation of the main system components, which is an improvement over the steady-state assumptions used in other reviewed studies. Consequently, the work is relevant not only for hybrid CAES-CSP systems but also for each technology individually, offering designs for an optimized high-efficiency OVAR and an innovative air reservoir suitable for small-scale CAES applications.

2. System Description

This section presents the prototype detailing its design and technical specifications and operating modes. The system is currently being installed at CIEMAT-Plataforma Solar de Almería, Spain. The prototype is an extended research prototype that was originally implemented during the CAPTure Horizon 2020 project [36].

2.1. Previous Project CAPTure: Upgrading the Existing Prototype

The CAPTure project lasted from May 2015 to July 2020 and focused on an OVAR-based CSP plant configuration that included a regenerative system—composed of two chambers—coupling the high-temperature atmospheric air stream with the pressurized air loop of the topping Brayton cycle. A 300 kW$_{th}$ prototype was implemented, connecting the solar receiver [22,37] with the regenerative heat exchange system and a small-scale Brayton cycle. Figure 1a presents a three-dimensional view of the CAPTure validation prototype, while Figure 1b shows the 45 m solar tower during on-sun testing, where the complete prototype was installed at the top. Unfortunately, the turbine start-up was not achieved during the CAPTure project due to several problems and limited testing time [36].

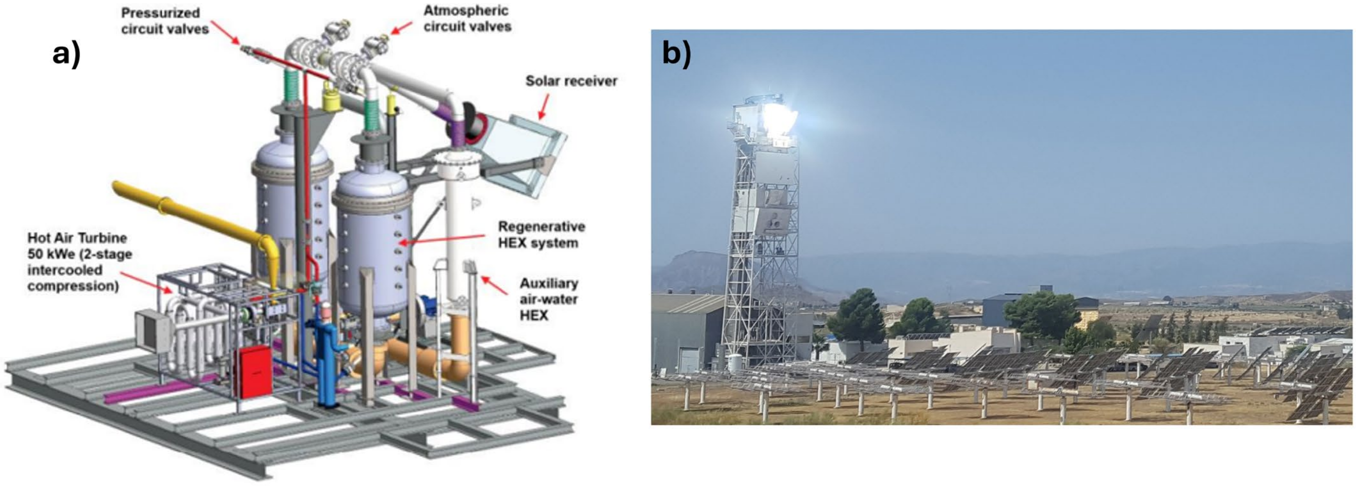

Figure 1. (**a**) CAPTure validation prototype 3-D view (CSP with regenerative HEX). (**b**) Solar tower at CIEMAT-PSA with CAPTure OVAR during on-sun testing. Adapted from [13].

The ASTERIx-CAESar project is currently upgrading the existing prototype by incorporating a small-scale CAES unit to demonstrate the operation of the integrated CAES-CSP concept. In particular, the CAPTure receiver is being enhanced, and the regenerative system has been replaced with a conventional shell-and-tube heat exchanger. The CAPTure hot air turbine has been downsized to a two-stage hot air expander, and the system at the top of the tower was supplied with compressed air from the CAES unit installed at the base of the tower. In addition, a reverse osmosis unit was pneumatically driven by the CAES system; however, the detailed design of the desalination unit lies outside the scope of the present study.

2.2. Layout and Operation Modes

Figure 2 shows a simplified schematic of the prototype, identifying the main subsystems and four operating modes. In the first mode “receiver only operation”, the solar receiver loop enables standalone testing of the OVAR at thermal powers of up to 500 kW_{th}, with the hot air subsequently cooled by an air-water heat exchanger. In the "compressor operation", the subsystem is located at the ground level, where the compressor charges the compressed air storage system. Furthermore, the "turbine warm-up" mode comprises an auxiliary blower that drives hot air at ambient pressure through the turbine. Finally, during "turbine operation", compressed air from the CAES system is released, heated in a 200 kW_{th} air-air heat exchanger using solar thermal energy, and expanded in the turbine. The corresponding piping and instrumentation diagram (P&ID) of the prototype is included in Section 5.

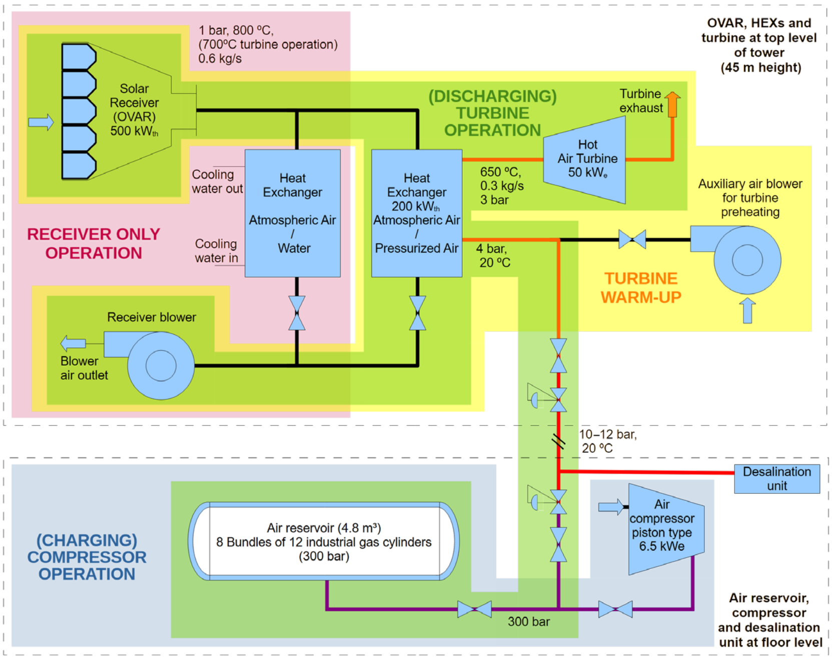

Figure 2. Simplified prototype layout and operation modes. Adapted from [13].

Figure 3a presents a three-dimensional model of the CAES-CSP prototype to be installed at the top of the tower, including the OVAR, heat exchangers, and turbine, while Figure 3b shows the components installed at the base of the tower, namely the air reservoir, compressor, and desalination unit.

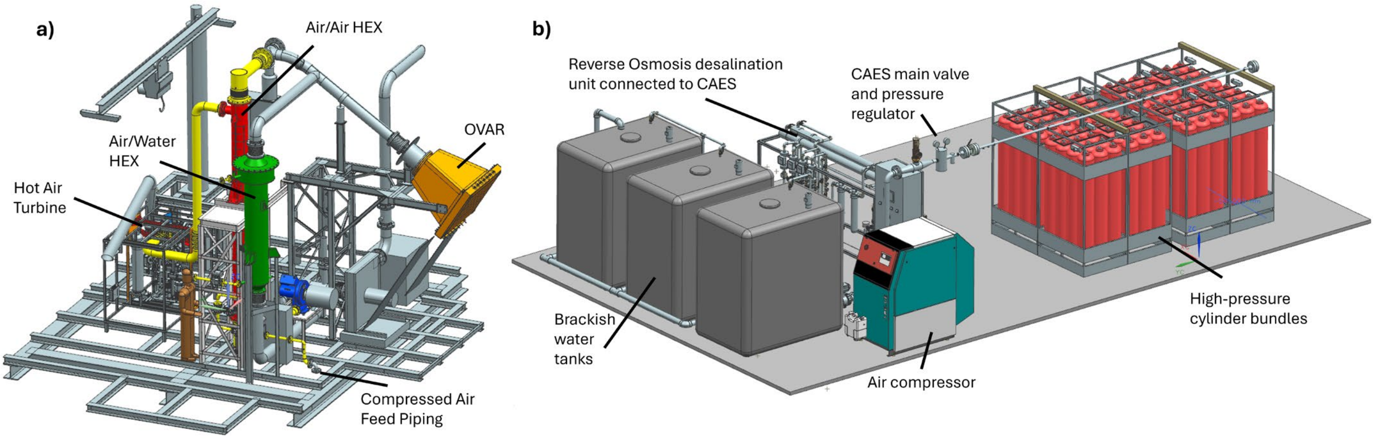

Figure 3. (**a**) 3-D model of the CAES-CSP prototype at the top of the tower and (**b**) 3-D model of the CAES-CSP prototype at the bottom of the tower. Adapted from [13].

3. Open Volumetric Air Receiver

3.1. Description and Modeling

The OVAR concept is designed as a modular system, composed of multiple identical modules stacked on top of each other, consisting of a ceramic foam absorber—made of porous Silicon-Infiltrated Silicon Carbide (SiSiC)—and a ceramic cup, manufactured from a novel lightweight composite material, which holds the absorber in place and guides the airflow [37]. In contrast to the CAPTure project, in which modules of 14 cm × 14 cm were installed, a larger optimal module size has been defined to reduce costs while maintaining adequate mechanical stress resistance. Consequently, in the present prototype, the receiver area of 0.69 m^2 is divided into 16 modules of 24.65 cm × 17.5 cm (see Figure 4). This study investigates the optimization of a passive mass flow regulation technique designed to enhance thermal efficiency. In CSP plants, heliostat pointing strategies that minimize spillage lead to non-uniform solar flux distributions across the receiver. This non-uniformity penalizes overall efficiency, as modules in the peripheral regions receive lower flux and, for similar mass flow rate, exhibit lower outlet temperatures. Furthermore, because air viscosity increases with temperature, the hotter central regions experience higher flow resistance. This leads to a reduction in mass flow through the hottest modules, further increasing their temperature and exacerbating the thermal gradient [38]. To mitigate this effect and achieve a more uniform outlet temperature distribution, the mass flow rate in the peripheral modules must be restricted. To this end, this study analyzes a passive mass flow control strategy based on the proportional reduction in the outlet orifice diameter of individual modules, thereby increasing their pressure drop and promoting a more balanced temperature distribution. By reducing the mass flow rate through the lower-flux peripheral modules, the orifices increase their air temperature rise, allowing their outlet temperatures to remain closer to the receiver outlet temperature setpoint.

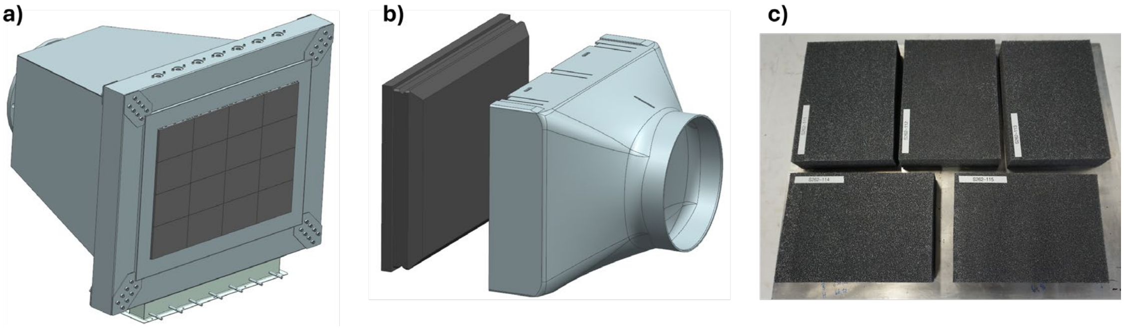

Figure 4. (**a**) 500 kW_{th} receiver design composed of 16 modules, each measuring 24.65 cm × 17.5 cm. (**b**) Rear view of one unassembled module consisting of a ceramic foam absorber and one cup. (**c**) Photograph of ceramic foam absorbers awaiting installation in the receiver front frame.

This analysis is based on a one-dimensional Modelica model using a local thermal non-equilibrium approach, which accounts for the exponential attenuation of solar flux within the foam. The thermal model of a single module had been previously validated against experimental data. The comparison between numerical and experimental air outlet temperatures yielded an RMSE of 16.9 °C, corresponding to a normalized RMSE of 2.2%. Further details on the validation procedure are available in the literature [21,37]. The model was subsequently extended to discretize the receiver area into the 16 individual modules, thereby accounting for non-uniform solar flux distributions. Based on a mesh sensitivity analysis, the foam and cup domains have been discretized axially into 15 and five nodes, respectively. The mass flow rate through each module, i, is determined as a function of its corresponding pressure drop. Within this framework, the total receiver mass flow rate, $\dot{m}_{rec}$, is calculated as the sum of the individual module contributions, $\dot{m}_{m,i}$:

$$\dot{m}_{rec} = \sum_{i=1}^{16} \dot{m}_{m,i} \tag{1}$$

Since the modules are arranged in parallel, they share a common pressure drop, ΔP_m:

$$\Delta P_m = \Delta P_{foam,i} + \Delta P_{cup,i} \ \ \forall i = 1, \ldots, 16 \tag{2}$$

where $\Delta P_{foam,i}$ is the pressure drop across the ceramic foam section of cup i, obtained by summing the contributions of the 15 discretized axial nodes j [39]. Each node has a thickness $t_{foam,j}$. The pressure drop is calculated from viscous and inertial terms, which depend on the foam pore diameter d, porosity ε, dynamic viscosity $\mu_{i,j}$, density $\rho_{i,j}$, and superficial velocity $v_{i,j}$ at node j:

$$\Delta P_{foam,i} = \sum_{j=1}^{15} \left(\frac{(1039 - 1002\varepsilon)}{d^2} \mu_{i,j} v_{i,j} + \frac{0.5138\varepsilon^{-5.739}}{d} \rho_{i,j} v_{i,j}^2 \right) \cdot t_{foam,j} \ \ \forall i = 1, \ldots, 16 \tag{3}$$

The term $\Delta P_{cup,i}$ represents the pressure drop associated with the cup geometry:

$$\Delta P_{cup,i} = K_i \frac{1}{2} \rho_{m,i} v_{m,i}^2 \quad \forall i = 1, \ldots, 16 \tag{4}$$

where K_i is the dimensionless pressure loss coefficient associated with the outlet orifice geometry of cup i, and $v_{m,i} = \frac{\dot{m}_{m,i}}{\rho_{m,i} A_m}$ is the flow velocity evaluated at the cup inlet (foam outlet) cross-section, A_m. Therefore, the pressure-loss coefficient, K_i was treated as geometry-dependent for each fixed orifice, while the effects of operating conditions were accounted for through the air properties and dynamic pressure in the pressure drop calculation. Finally, the global receiver pressure drop, ΔP_{rec}, includes additional resistance from the receiver box, ΔP_{box}, calculated in CAPTure project with Computational Fluid Dynamics (CFD) simulations:

$$\Delta P_{box} = 9.8573 + 21.451 \dot{m}_{rec} + 1730.8 \dot{m}_{rec}^2 \tag{5}$$

$$\Delta P_{rec} = \Delta P_m + \Delta P_{box} \tag{6}$$

Additionally, the thermal model was integrated with a Proportional-Integral-Derivative controller (PID) controller to adjust the overall mass flow rate to obtain a receiver outlet temperature of 800 °C in each simulation.

To accurately characterize the pressure losses associated with the cup geometry, CFD simulations were carried out using Ansys Fluent 2024 R1. The pressure drop coefficient, K_i, was evaluated for orifice diameters ranging from 35 mm to 122 mm, corresponding to the external cup opening. The simulations employed the shear stress transport (SST) $k - w$ turbulence model and were performed under varying operating conditions, including inlet velocities between 1 and 3 m/s and temperatures from 400 to 800 °C. For each configuration, three simulations were conducted, yielding a maximum deviation of 2% in the calculated K_i values, confirming the assumption of a constant pressure drop coefficient within the investigated range. This deviation has a negligible influence on the results. Figure 5 compares the velocity field distributions for 35 mm and 100 mm orifice diameters, highlighting the effect of orifice size at an inlet velocity of 1.5 m/s and a temperature of the air of 800 °C. Figure 6 shows the variation in the pressure drop coefficient, K_i, as a function of the orifice diameter.

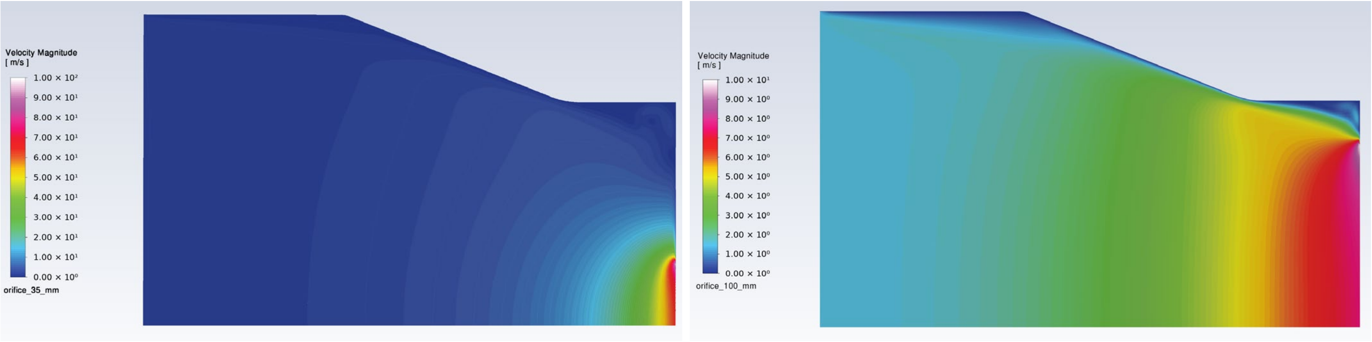

Figure 5. Velocity field distributions for 35 mm and 100 mm orifice diameters, showing how orifice size modifies the flow pattern and outlet acceleration within the cup geometry, shown in the vertical symmetry plane.

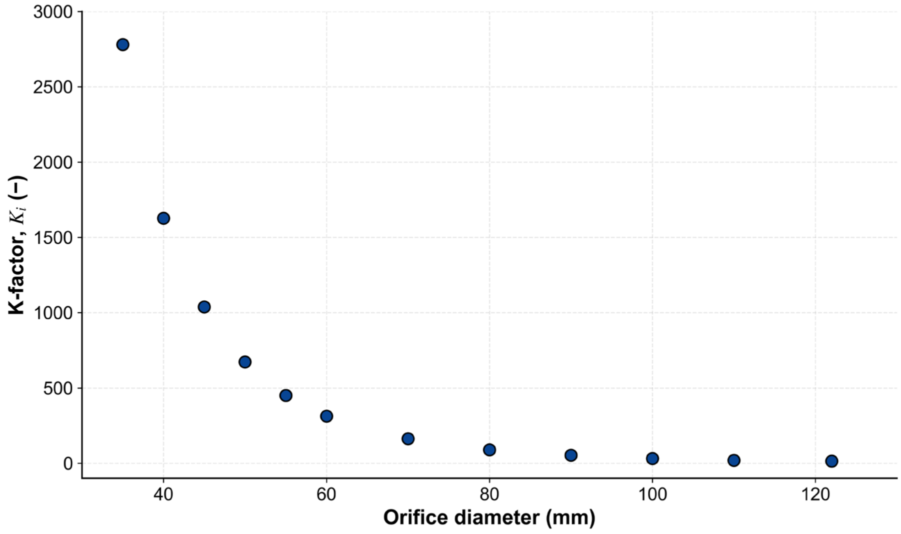

Figure 6. Pressure drop coefficient, K_i, as a function of the cup orifice diameter obtained from CFD simulations.

Finally, the optimization is conducted to maximize the thermal energy efficiency of the overall receiver, η_{rec}:

$$\eta_{rec} = \frac{\dot{Q}_{th}}{I_{rec}} = \frac{\dot{m}_{rec}\left(h_{rec,out} - h_{rec,in}\right)}{\sum_{i=1}^{16} I_{m,i} A_m} \tag{7}$$

where $\dot{Q}_{th}$ is the useful thermal power absorbed by the fluid, I_{rec} is the total incident radiative power on the receiver, $h_{rec,out}$ and $h_{rec,in}$ are the specific enthalpies of the fluid at the receiver outlet and inlet, respectively, and $I_{m,i}$ is the local radiative heat flux incident on cup i.

3.2. *Optimization for Non-Homogeneous Solar Flux*

Flux measurements obtained during the CAPTure project at PSA in June 2020 were used to construct a representative symmetric solar flux map with elevated flux levels. A Gaussian distribution was then assumed to reproduce the corresponding spatially non-uniform flux profile incident on the receiver surface, consistent with the steady-state nominal conditions expected during the experimental campaign.

Figure 7a illustrates the reference (base-case) solar flux distribution, while Figure 7b presents the discretized flux values, $I_{m,i}$, assigned to each cup, with a total solar flux of

$I_{rec} = 625.7$ kW. For the specific base-case configuration considered, four distinct flux input levels can be identified among the cups, allowing the corresponding outlet orifice sizes to be optimized: $\varnothing_A$, $\varnothing_B$, $\varnothing_C$, while $\varnothing_D$ is fixed at the maximum outlet diameter of 122 mm.

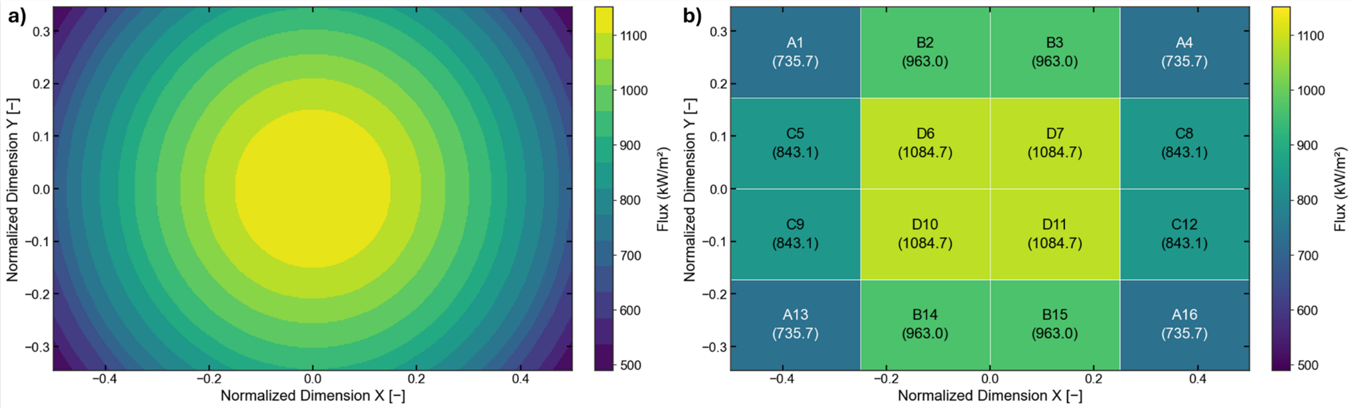

Figure 7. (**a**) Symmetric representative solar flux map on receiver, derived from CAPTure measurements and (**b**) corresponding discretized flux distribution applied to individual receiver cups.

A parametric analysis was conducted to evaluate all feasible configurations constrained by the discretized cup orifice diameters shown in Figure 6 and satisfying the condition $\varnothing_A \leq \varnothing_C \leq \varnothing_B \leq \varnothing_D$. For clarity, Figure 8 shows only the high-performing subset of configurations, defined here as those achieving receiver thermal efficiencies above 77%. The results are grouped in three diagrams according to the values of $\varnothing_A$,$\varnothing_B$,$\varnothing_C$, respectively; therefore, each diagram represents the same subset of configurations but ordered by a different orifice diameter. The maximum thermal efficiency is obtained for $\varnothing_A = 60$,$\varnothing_B = 80$,$\varnothing_C = 70$ and $\varnothing_D = 122$ mm. Under this configuration, a thermal efficiency of 81.6% is achieved, representing a predicted improvement of 7.7% over the simulated baseline case obtained without the passive mass flow rate regulation technique ($\eta_{rec} = 75.8\%$).

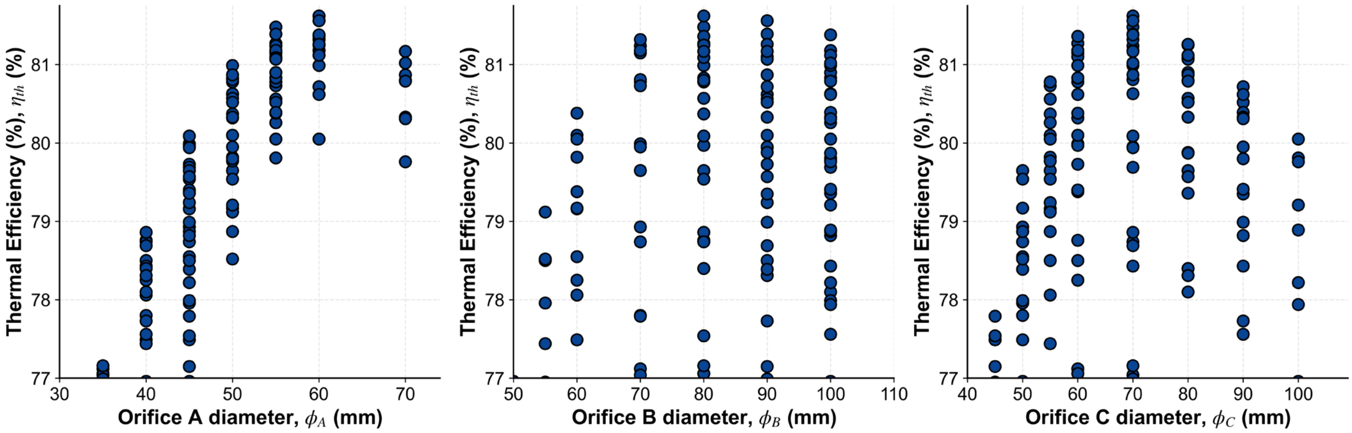

Figure 8. Parametric study to obtain the maximum receiver thermal efficiency achieved for discrete orifice diameters across configurations $\varnothing_A$, $\varnothing_B$ and $\varnothing_C$.

Table 3 presents the thermal performance of each cup within the optimum configuration. The deviation of the module outlet temperature relative to the overall receiver target temperature of 800 °C is only 4.9%, confirming a high degree of thermal uniformity among all cups. The pressure drop across the modules is $\Delta P_m = 0.70$ kPa, with a total pressure drop of $\Delta P_{rec} = 1.38$ kPa when the downstream box is included.

Table 3. Simulated performance of optimum configuration receiver at the base-case solar flux conditions.

Module	Outlet Orifice, Ø (mm)	Incident Power (kW)	Mass Flow Rate, $\dot{m}_{m,i}$ (kg/s)	Outlet Temperature (°C)	Thermal Efficiency, η_{rec} (%)	Pressure Drop Foam, $\Delta P_{foam,i}$ (Pa)	Pressure Drop Cup, $\Delta P_{cup,i}$ (Pa)
A1-A4-A13-A16	60	31.7	0.033	765.4	81.5	441.4	263.6
B2-B3-B14-B15	80	41.5	0.039	833.5	81.3	591.3	113.6
C5-C8-C9-C12	70	36.4	0.038	760.6	82.2	519.7	185.3
D6-D7-D10-D11	122	46.8	0.044	833.3	81.9	681.8	23.1

3.3. Transient Operation

Once the receiver configuration is optimized, the dynamic model has been employed to simulate transient operating performance using a different set of measured operating conditions from the same June 2020 CAPTure campaign. They do not represent the final optimized aiming strategy of the new prototype, which will be defined to reproduce the design flux distribution as closely as possible. This approach enables the assessment of the system under realistic off-design operating scenarios, which are representative of actual solar field variability. In this way, the model is not limited to design point evaluation, but is used to assess operational robustness, thermal response, and control performance under dynamic conditions. This distinction between design and operational conditions is essential in solar-driven systems, where continuous deviations from nominal operation are expected.

Figure 9 shows the variation in the incident flux on each module. It can be observed that the heliostat aiming strategy on that case exhibited an asymmetric distribution shifted toward the left-side modules, with significant flux differences among cups of the same type.

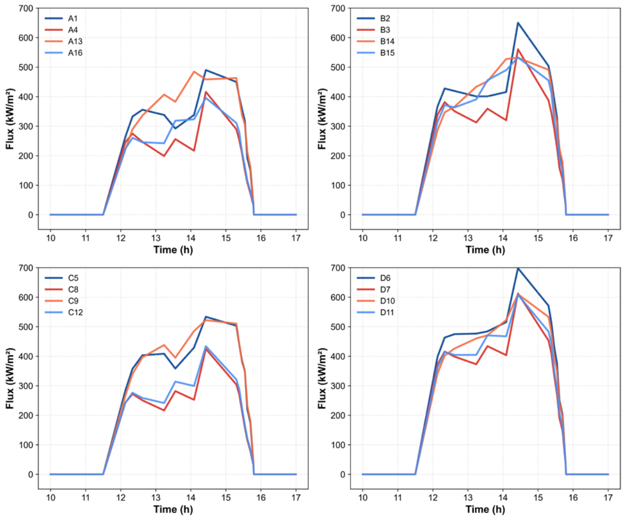

Figure 9. Transient operating conditions. Evolution of incident solar flux across individual modules.

Figure 10 shows the outlet temperature of each module. During start-up, a proper temperature increase is observed, followed by fluctuating thermal behavior throughout the day, associated with transient solar input and heliostat aiming conditions. During operation, temperatures range from 388 °C to 1248 °C, with significant differences among the A-type and C-type modules due to variations in the incident solar flux. The maximum values remain below, but close to the allowable material limits (∼1350 °C) of the modules. These results highlight the importance of an adequate heliostat aiming strategy to reduce thermal non-uniformities and to maintain operating conditions close to design values.

Additionally, they underscore the importance of module outlet temperature monitoring for preventing receiver overheating during solar transients.

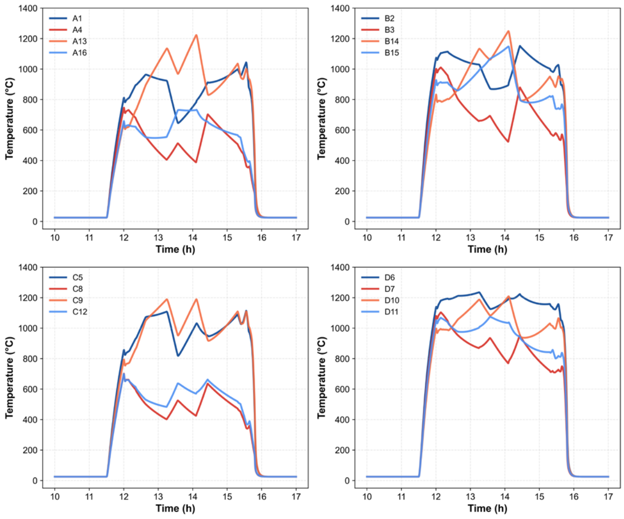

Figure 10. Transient operating conditions. Evolution of outlet temperature across individual modules.

Finally, Figure 11 summarizes the performance of the overall receiver, including the total incident flux, mass flow rate, and outlet receiver temperature. The maximum incident power, 366 kW, remains below the prototype design point but corresponds more closely to the turbine operating mode, thus representing the off-design conditions expected during the entire experimental campaign. The mass flow rate is adjusted, with controlled thermal inertia, to regulate the outlet temperature within 795–855 °C. The thermal efficiency remains in the range of 64.9–75.3%. These results reflect the system response under reduced solar input and non-ideal operating conditions. The model proves to be a useful tool for operating the prototype during the upcoming experimental campaign, supporting operational planning and control strategy definition under transient irradiance conditions.

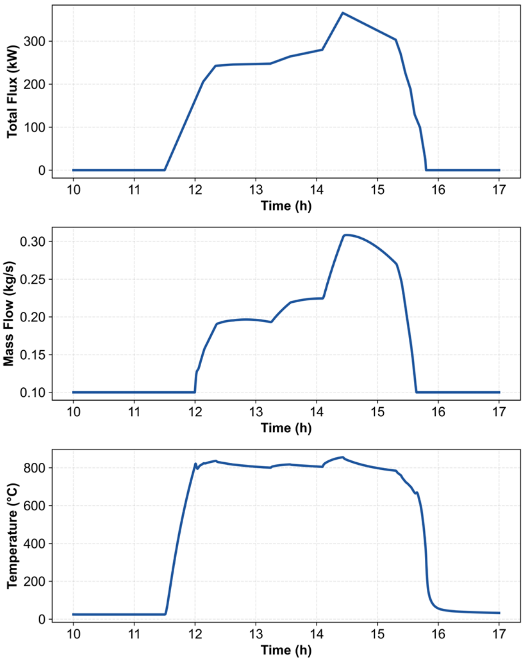

Figure 11. Transient operating conditions. Evolution of overall receiver performance: total solar flux, mass flow rate, and outlet temperature.

4. Air Reservoir

4.1. Aboveground Storage Solutions

Regarding CAES, for small-scale and micro-scale systems, air is typically stored in aboveground reservoirs. Previous studies on micro-scale CAES prototypes report storage pressures ranging from 7 to 350 bar, reservoir volumes between 0.25 and 750 m^3, and discharge durations from 0.8 to 15 h [6]. Based on these values, the present prototype is designed to deliver a nominal discharge mass flow rate of 0.3 kg/s, corresponding to an electrical output of 50 kW_e and a discharge duration exceeding 75 min. This results in a total discharged air mass of approximately 1350 kg.

Aboveground air storage systems are available in a wide range of configurations depending on the application requirements. The most common solutions include custom-designed large steel pressure vessels [30,31,35], arrays of high-pressure pipelines assembled on skids, and interconnected bundles of industrial high-pressure gas cylinders [32,34,40] (see Figure 12).

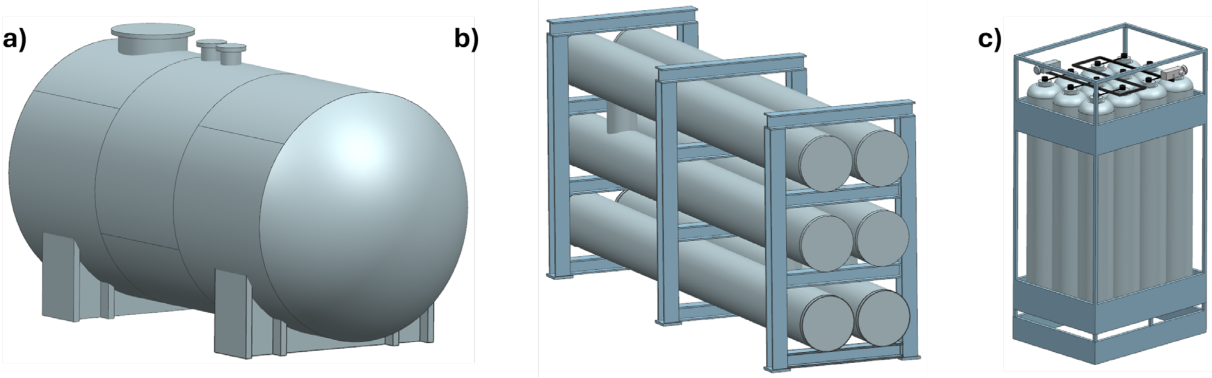

Figure 12. Comparison of aboveground air storage solutions for small-scale CAES: (**a**) steel pressure vessel (165 bar, 8.2 m^3), (**b**) skid-mounted pipelines (165 bar, 8.2 m^3), (**c**) and bundles of high-pressure gas cylinders (300 bar, only one bundle of 0.6 m^3).

To identify the most suitable option, several quotations were requested from manufacturers of pressure vessels and suppliers of standard high-pressure gas cylinders. Increasing the maximum storage pressure reduces the required storage volume but leads to thicker vessel walls. Therefore, an optimal pressure level exists for custom-designed steel pressure vessels. In addition, pressure vessels are subject to strict regulatory requirements in many countries and must comply with certification and inspection procedures established by authorized bodies, as well as safety standards such as ASME or PED [41].

Figure 13 summarizes the commercial quotations received as a function of maximum pressure. Although increasing the storage pressure reduces the required reservoir volume, pressure vessel manufacturers proposed maximum operating pressures in the range of 150–165 bar as a feasible solution in terms of structural thickness and manufacturability, corresponding to storage volumes of approximately 8–9 m^3. In contrast, commercial gas cylinders allow storage pressures of up to 200–300 bar while maintaining relatively low costs. These cylinders typically have a volume of 50 L and can be supplied in bundled configurations, interconnected through small-diameter high-pressure piping, which accounts for approximately 5% of the total cost. The configuration of 300 bar represents the most cost-effective solution and was therefore selected for the prototype scale.

Therefore, for micro-scale CAES systems, modular high-pressure gas cylinders are the preferred solution due to their low cost, mass production advantages, and simple interconnection. However, as storage requirements grow toward medium-scale plants, multiplying small vessels quickly becomes impractical due to space, installation, and balance-of-plant constraints. Consequently, alternative storage solutions, such as repurposed infrastructure or underground storage, become more relevant at larger scales, where techno-economic performance must be carefully reassessed.

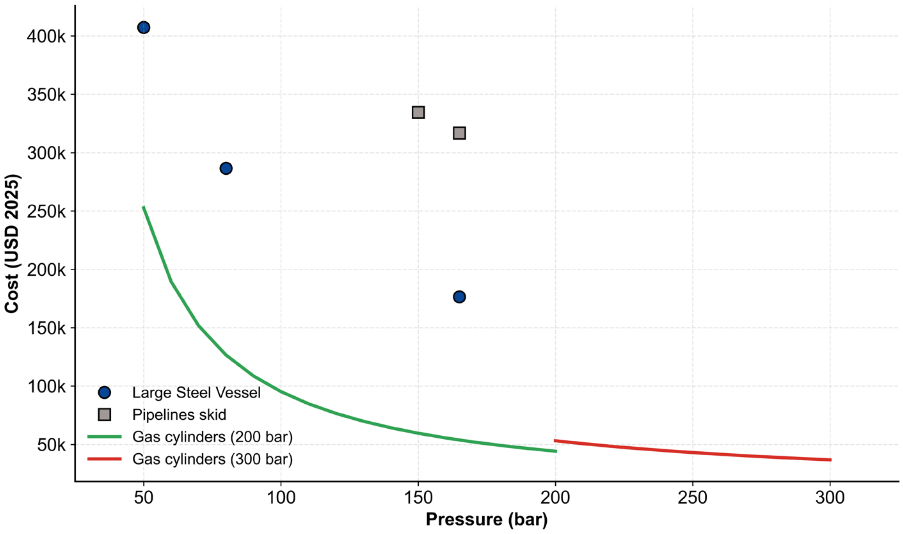

Figure 13. Commercial quotations (USD 2025) for air storage options for the prototype, showing the relationship between maximum operating pressure and cost for different technologies.

4.2. Modeling and Discharging Simulation

This section presents a more detailed analysis of the air reservoir discharge process, which is essential for accurately predicting the evolution of temperature and pressure. These variables are key parameters for determining the actual operating duration and conditions of the prototype. Pressure regulation during discharge is governed by the Joule–Thomson effect, resulting in a significant temperature drop due to air expansion.

To capture these dynamics, the discharging process was modeled in Modelica, simulating the transient energy and heat balances of the air reservoir. As reported in the literature [14,40], assuming ideal gas behavior introduces error, as it slightly underestimates the rates of temperature and pressure decrease during the discharge process. Therefore, real gas properties for dry air were employed, obtained from the LibHuAir library [42]. The energy balance within the reservoir also accounts for convective heat transfer at the cylinder walls, both internal and external, using experimentally determined heat transfer coefficients of $h_{conv,\,in}$ = 25.42 W/m^{2}K and $h_{conv,\,ext}$ = 2.47 W/m^{2}K [34]. Heat transfer by radiation is considered negligible [34], and, due to the large surface area, the initial temperature of the air reservoir is assumed equal to the ambient temperature. The outlet pressure downstream of the regulator/throttling valve is set to 10 bar.

Figure 14 illustrates the temporal evolution of pressure and temperature during the discharging process for ambient temperatures of 20, 30, and 40 °C. The simulation results indicate a total storage volume of 4.8 m^3 required to discharge the reservoir from 300 bar down to the minimum pressure of 20 bar over the required duration of more than 75 min. The final design consists of eight bundles of twelve 50 L cylinders each (see Figure 15).

For initial ambient temperatures of 20 and 30 °C, it is observed that the regulator outlet temperature reaches significantly low values during expansion. Although the air filter of the compressor ensures nearly dry air, these temperature drops may still promote ice formation at the throttle valve, potentially leading to flow obstruction [40]. To mitigate this risk, thermal management strategies may be required, such as immersing the gas cylinders in a temperature-controlled water bath or applying industrial heating blankets to the valve assembly in order to prevent icing and ensure stable operation.

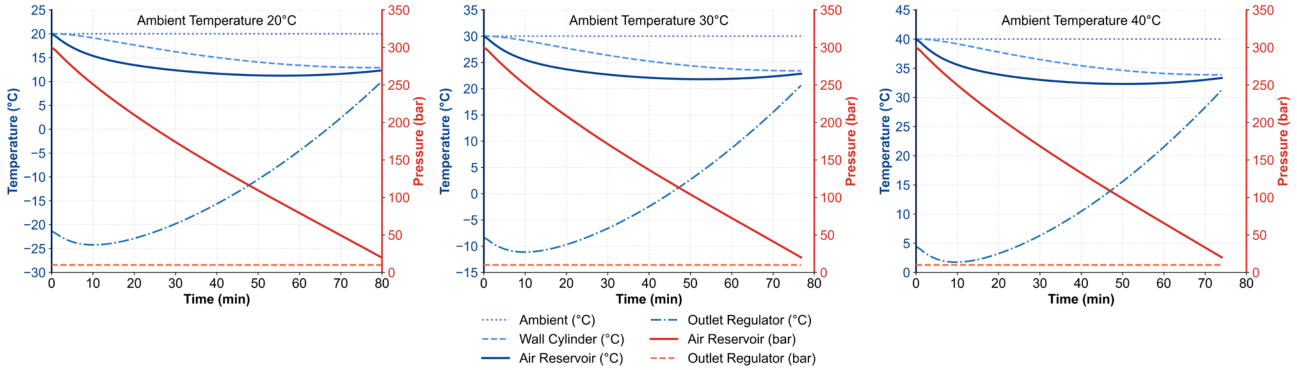

Figure 14. Modeled discharging operation of the air reservoir: temperature and pressure profiles as a function of ambient temperature.

Figure 15. Bundles of high-pressure gas cylinders awaiting interconnection in the prototype CAES system. Some bundles are partially hidden from view.

5. Other Components Selection and P&ID

In addition to the main prototype components—namely the OVAR and the air reservoir—the prototype incorporates several key components that have been carefully selected to meet operational requirements. The air-air heat exchanger, which replaces the regenerative heat exchanger (HEX) of the CAPTure prototype, is a 200 kW_{th} shell-and-tube unit constructed of AISI 309, with a heat exchange area of 56 m^2.

The CAES charging process is performed using a standard industrial piston-type air compressor, Bauer PE 120-7.5-VE (BAUER KOMPRESSOREN Ibérica, S.L., Sant Esteve Sesrovires, Spain), selected for its compactness, low cost, simple design, and widespread industrial use, despite its relatively low efficiency and power capacity [6]. The compressor provides a limited volumetric flow of 15.6 m^3/h. To ensure dry air for CAES charging, the compressor is equipped with a refrigeration dryer, Bauer B-KOOL 680 (BAUER KOMPRESSOREN Ibérica, S.L., Sant Esteve Sesrovires, Spain) and an additional air filter.

Discharge is controlled through a dome pressure regulator HORNUNG G 1 1/2″ (Iberfluid Instruments S.A., L'Hospitalet de Llobregat, Spain), which reduces the reservoir pressure to an intermediate level. A secondary pressure reducer SAMSON Type 41-23 (SAMSON S.A.U., Rubí, Spain) further adjusts the pressure to the turbine inlet conditions. This two-stage regulation ensures stable operation and appropriate matching of turbine inlet requirements. The exact pressure drop and response time will depend on the operating point and will be quantified during commissioning. Pressure sensors will be installed upstream and downstream of the regulators and at the turbine inlet to monitor operation. The hot air turbine is a bespoke design, based on a modified small-scale Brayton cycle using radial turbomachinery from repurposed truck turbocharger components. The first expansion stage corresponds to the turbocharger, with the outlet air from the compressor stage simply vented to the environment. This configuration provides an economical approach for demonstrating air expansion at small scale.

Piping is equipped with several axial expansion joints to accommodate thermal expansion. Pipe diameters were designed according to recommended flow rates for compressed air pipelines [41] and high-pressure hose specifications, limiting the velocity to 25 m/s. This limit is locally exceeded in some sections toward the end of the discharge period; however, this does not affect operation given the short-term experimental nature of the prototype.

Figure 16 presents the piping and instrumentation diagram (P&ID). An extensive instrumentation layout is implemented across the facility to assess system behavior and control performance. Approximately 40 sensors are distributed throughout the installation to monitor key operating variables, including pressure, temperature, and mass flow rates.

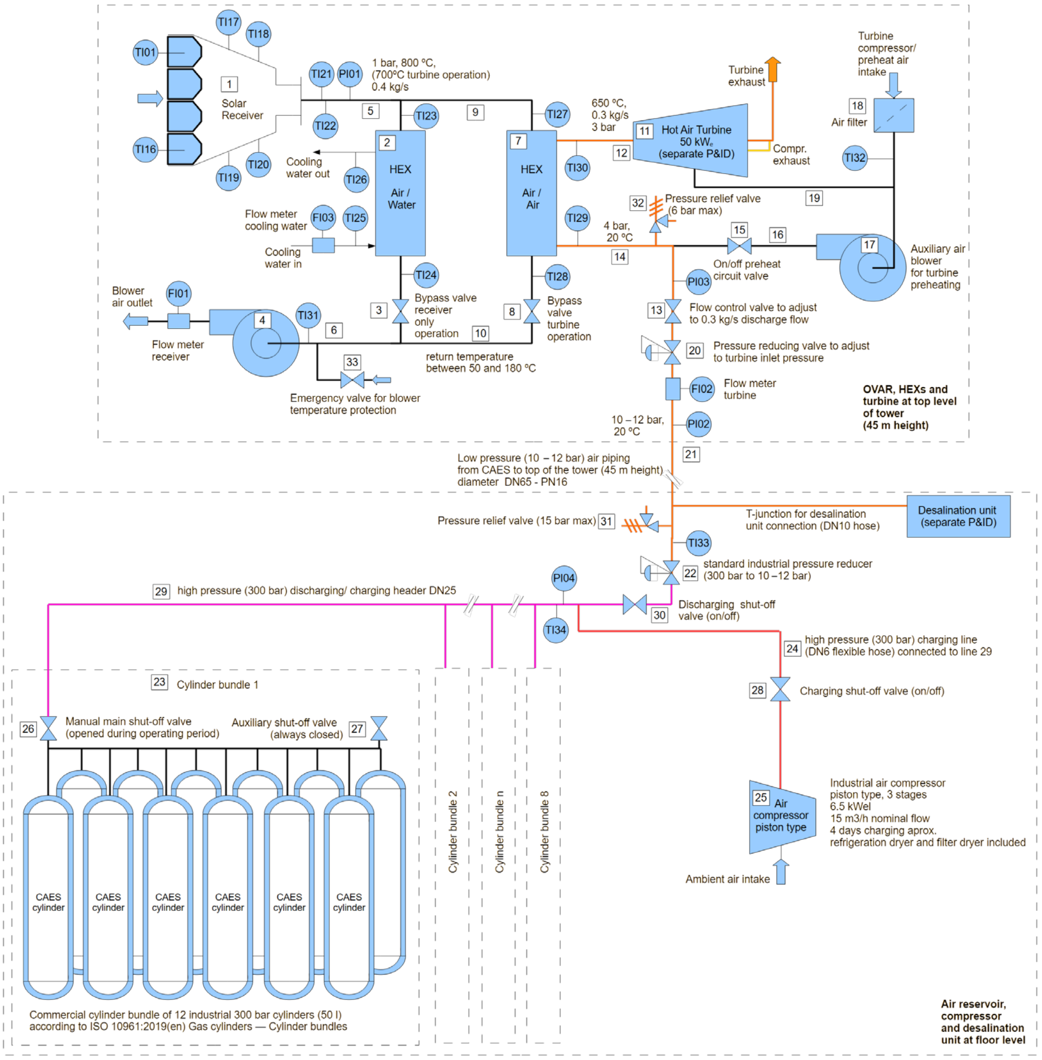

Figure 16. Piping and instrumentation diagram (P&ID) of the prototype, showing components located at both the top and base of the solar tower. Adapted from [13].

6. Conclusions

This study presents the design and modeling of an experimental prototype combining an air-based high-temperature CSP receiver integrated with a CAES system. The main findings are summarized as follows:

- A complete system architecture is developed and described, including operating modes, control strategies, and component-level integration of the main CSP and CAES subsystems.
- The solar receiver was designed using a modular discretization approach, combining thermal modeling and pressure drop estimation to optimize passive mass flow regulation. Under design conditions of 500 kW_{th} and 800 °C outlet temperature, simulations resulted in a thermal efficiency of 81.6%, corresponding to a 7.7% improvement relative to the predicted non-regulated baseline case.
- Transient simulations of the OVAR under experimentally derived off-design conditions demonstrate the capability of the model to reproduce system-level thermal behavior, including mass flow redistribution and outlet temperature control. The results highlight the sensitivity of system performance to solar flux distribution and flow regulation, providing relevant insights for experimental operation, heliostat aiming and control strategy development.
- A techno-economic comparison of aboveground storage options identifies high-pressure (300 bar) gas cylinders as the most cost-effective solution. Discharge simulations indicate a required storage volume of 4.8 m^3.
- The integrated design, including auxiliary components and instrumentation defined through the P&ID, provides a robust experimental framework for system monitoring and control during operation.

Future work will focus on experimental validation at CIEMAT-Plataforma Solar de Almería under real solar-driven conditions. This campaign will assess prototype operation at Technology Readiness Level (TRL) 6–7, validate the dynamic models, evaluate scalability, and support future techno-economic studies of larger CAES-CSP systems.

Author Contributions: Conceptualization, J.B. and F.Z.; methodology, J.B. and F.Z.; software, J.B. and X.R.; validation, X.R., L.C.A.-P., A.L.Á.-M. and F.Z.; investigation, J.B.; resources, R.P., A.L.Á.-M. and F.Z.; data curation, J.B.; writing—original draft preparation, J.B.; writing—review and editing, J.B., X.R., R.P., L.C.A.-P., A.L.Á.-M. and F.Z.; visualization, J.B.; supervision, F.Z.; project administration, F.Z.; funding acquisition, F.Z. All authors have read and agreed to the published version of the manuscript.

Funding: This research was funded by the European Union's Horizon Europe research and innovation program under project "ASTERIx-CAESar" with grant agreement No. 101122231.

Data Availability Statement: The raw data supporting the conclusions of this article will be made available by the authors on request.

Acknowledgments: The authors gratefully acknowledge the collaboration of David Astrain. During the preparation of this manuscript/study, the author(s) used ChatGPT-4 for the purposes of language polishing and improving the readability of the manuscript. The authors have reviewed and edited the output and take full responsibility for the content of this publication.

Conflicts of Interest: The author Rafael Pérez is employed by the company Aalborg CSP A/S, Aalborg, Denmark. The remaining authors declare that the research was conducted in the absence of any commercial or financial relationships that could be construed as a potential conflict of interest.

Abbreviations

The following abbreviations are used in this manuscript:

CAES	Compressed Air Energy Storage
CSP	Concentrated Solar Power
OVAR	Open Volumetric Air Receiver
P&ID	piping and instrumentation diagram

D-CAES	Diabatic Compressed Air Energy Storage
A-CAES	Adiabatic Compressed Air Energy Storage
T-CAES	Trigenerative Compressed Air Energy Storage
TES	Thermal Energy Storage
PID	Proportional-Integral-Derivative controller
SiSiC	Silicon-Infiltrated Silicon Carbide
CFD	Computational Fluid Dynamics
SST	shear stress transport
ASME	American Society of Mechanical Engineers
PED	Pressure Equipment Directive
HEX	heat exchanger
TRL	Technology Readiness Level

References

1. IRENA. *Renewable Energy Statistics 2025*; International Renewable Energy Agency: Masdar City, Abu Dhabi, 2025.
2. Khan, S.H. Energy storage systems for deep decarbonization: A critical review. *J. Energy Storage* **2026**, *150*, 120485. [CrossRef]
3. Olabi, A.G.; Wilberforce, T.; Ramadan, M.; Abdelkareem, M.A.; Alami, A.H. Compressed air energy storage systems: Components and operating parameters—A review. *J. Energy Storage* **2021**, *34*, 102000. [CrossRef]
4. Zhang, R.; Zhao, G. A comprehensive review of compressed air energy storage technologies: Current status and future trends. *J. Renew. Sustain. Energy* **2025**, *17*, 022702. [CrossRef]
5. Tumminello, D.; Bacci, T.; Facchini, B.; Stortiero, F.; Castelli, G. Numerical modeling and exergetic analysis of efficiency improving solutions for a micro-CAES system. *J. Phys. Conf. Ser.* **2023**, *2648*, 012045. [CrossRef]
6. Zheng, Y.; Guo, H.; Zhang, H.; Guo, W.; Zhao, M.; Xu, Y.; Huang, J.; Chen, H. A review of micro compressed air energy storage: Applications, component selection, and dynamic modeling. *J. Energy Storage* **2025**, *137*, 118614. [CrossRef]
7. Crotogino, F.; Mohmeyer, K.-U.; Scharf, D.R. Huntorf CAES: More than 20 Years of Successful Operation. In Proceedings of the Solution Mining Research Institute (SMRI) Spring Meeting, Orlando, FL, USA, 15–18 April 2001.
8. Zhou, Y.; Zhang, H.; Liu, S.; Lu, Z.; Ding, X.; Duan, L.; Desideri, U. Experimental study on heat transfer characteristics between high-pressure air and molten salt used in solar-aided compressed air energy storage systems. *Energy* **2024**, *313*, 134127. [CrossRef]
9. Wei, Y.; Cheng, Z.; Zhang, H.; Zhou, Z.; Gao, Q.; Tian, Q. Optimal Dispatch of Multi-Energy Generation Systems Considering CSP and Advanced Adiabatic CAES. In Proceedings of the 2024 The 9th International Conference on Power and Renewable Energy (ICPRE), Guangzhou, China, 20–23 September 2024; pp. 912–917.
10. Bu, S.; Yang, X.; Sun, Y.; Li, W.; Su, C.; Wang, X.; Liu, X. Thermodynamic performances analyses and process optimization of a novel AA-CAES system coupled with solar auxiliary heat and organic Rankine cycle. *Energy Rep.* **2022**, *8*, 12799–12808. [CrossRef]
11. Saleh Kandezi, M.; Mousavi Naeenian, S.M. Thermodynamic and economic analysis of a novel combination of the heliostat solar field with compressed air energy storage (CAES); a case study at San Francisco, USA. *J. Energy Storage* **2022**, *49*, 104111. [CrossRef]
12. Baigorri, J.; Zaversky, F.; Astrain, D. Massive grid-scale energy storage for next-generation concentrated solar power: A review of the potential emerging concepts. *Renew. Sustain. Energy Rev.* **2023**, *185*, 113633. [CrossRef]
13. European Commission Air-Based Solar Thermal Electricity for Efficient Renewable Energy Integration & Compressed Air Energy Storage—ASTERIx-CAESar. Available online: https://cordis.europa.eu/project/id/101122231/es (accessed on 28 April 2026).
14. Baigorri, J.; Federici, A.; Kubikova, T.; Du Toit, T.; Rodríguez-deArriba, P.; Salvini, C.; Sánchez, D.; Zaversky, F. Modeling of an innovative integration of compressed air energy storage (CAES) with high-temperature concentrated solar power (CSP): A comprehensive use-case study. *J. Energy Storage* **2025**, *132*, 117678. [CrossRef]
15. Ávila-Marín, A.L. Volumetric receivers in Solar Thermal Power Plants with Central Receiver System technology: A review. *Sol. Energy* **2011**, *85*, 891–910. [CrossRef]
16. Moreno García-Moreno, J.; Milidonis, K. Generative Design of Concentrated Solar Thermal Tower Receivers—State of the Art and Trends. *Energies* **2025**, *18*, 5890. [CrossRef]
17. Hernández, B.; Ferber, N.L.; Abdullah, M.; Mayyas, A.; Calvet, N.; Chiesa, M. Central receiver-based CSP plants Part 2: Components categorization and future prospects. *Sol. Energy* **2025**, *299*, 113740. [CrossRef]
18. Zaversky, F.; Rández, X.; Baigorri, J.; Sánchez, M. The volumetric effect indicator—A new dimensionless characteristic number for the optimum design and operation of volumetric solar receivers. *Sol. Energy* **2023**, *259*, 119–129. [CrossRef]
19. Sanchez-Señoran, D.; Reyes-Belmonte, M.A.; Fernandez-Reche, J.; Avila-Marin, A.L. Numerical simulation of convective heat transfer coefficient in wire mesh absorbers with fixed porosity. *Results Eng.* **2023**, *17*, 100830. [CrossRef]
20. Cheilytko, A.; Schwarzbözl, P.; Wieghardt, K. Modeling of heat conduction processes in porous absorber of open type of solar tower stations. *Renew. Energy* **2023**, *215*, 118995. [CrossRef]

21. Zaversky, F.; Aldaz, L.; Sánchez, M.; Ávila-Marín, A.L.; Roldán, M.I.; Fernández-Reche, J.; Füssel, A.; Beckert, W.; Adler, J. Numerical and experimental evaluation and optimization of ceramic foam as solar absorber—Single-layer vs multi-layer configurations. *Appl. Energy* **2018**, *210*, 351–375. [CrossRef]
22. Zaversky, F.; Les, I.; Füssel, A.; Valentin, B.; Avila-Marin, A.L.; Beckert, W.; Aldaz, L. CAPTure Report on Model Development Including Detailed Model Validation (Deliverable 1.2). Available online: https://ec.europa.eu/research/participants/documents/downloadPublic?documentIds=080166e5d2272876&appId=PPGMS (accessed on 1 June 2026).
23. Guo, H.; Xu, Y.; Kang, H.; Guo, W.; Liu, Y.; Zhang, X.; Zhou, X.; Chen, H. From theory to practice: Evaluating the thermodynamic design landscape of compressed air energy storage systems. *Appl. Energy* **2023**, *352*, 121858. [CrossRef]
24. Tumminello, D.; Zuffi, C.; Bacci, T.; Facchini, B. Hybrid micro-compressed air energy storage with photovoltaic and diesel generation for off-grid applications: A parametric life cycle and techno-economic study. *Clean. Energy Syst.* **2026**, *13*, 100246. [CrossRef]
25. Matos, C.R.; Silva, P.P.; Carneiro, J.F. Overview of compressed air energy storage projects and regulatory framework for energy storage. *J. Energy Storage* **2022**, *55*, 105862. [CrossRef]
26. Institute of Engineering Thermophysics of the Chinese Academy of Sciences (IET-CAS) World's First 100-MW Advanced Compressed Air Energy Storage Plant Connected to Grid for Power Generation. 2026. Available online: https://english.cas.cn/Special_Reports/rd/2022/202410/t20241031_693356.shtml (accessed on 2 May 2026).
27. Seetao Jiangsu Salt Cavern Compressed Air Energy Storage Project Put into Operation. 2026. Available online: https://www.seetao.com/details/159902.html (accessed on 17 April 2026).
28. CleanTechnica China Developing World's Largest Compressed Air Energy Storage System 2026. Available online: https://cleantechnica.com/2024/12/26/china-developing-worlds-largest-compressed-air-energy-storage-system/ (accessed on 2 May 2026).
29. Energy Storage News Hydrostor Sees 1600M Wh Advanced Compressed Air Energy Storage Project in Australia Approved. 2026. Available online: https://www.energy-storage.news/hydrostor-sees-1600mwh-compressed-air-energy-storage-project-in-australia-approved/#: :text=The%20Silver%20City%20Energy%20Storage,)%20yesterday%20(25%20February) (accessed on 2 May 2026).
30. Zhang, X.; Gao, Z.; Zhou, B.; Guo, H.; Xu, Y.; Ding, Y.; Chen, H. Advanced Compressed Air Energy Storage Systems: Fundamentals and Applications. *Engineering* **2024**, *34*, 246–269. [CrossRef]
31. Tanveer, A.; Khan, F.; Usman, M.; Irfan, M.A. Design & Development of a Prototype Compressed Air Energy Storage Mechanism. In Proceedings of the 2022 International Conference on Emerging Trends in Electrical, Control, and Telecommunication Engineering (ETECTE), Lahore, Pakistan, 2–4 December 2022; pp. 1–6.
32. Cheayb, M.; Marin Gallego, M.; Tazerout, M.; Poncet, S. Modelling and experimental validation of a small-scale trigenerative compressed air energy storage system. *Appl. Energy* **2019**, *239*, 1371–1384. [CrossRef]
33. Maia, T.A.C.; Barros, J.E.M.; Cardoso Filho, B.J.; Porto, M.P. Experimental performance of a low cost micro-CAES generation system. *Appl. Energy* **2016**, *182*, 358–364. [CrossRef]
34. Dormoy, E.; Le Lostec, B.; Haillot, D. Aboveground compressed air energy storage systems: Experimental and numerical approach. *Energy Convers. Manag.* **2024**, *321*, 119073. [CrossRef]
35. Wang, S.; Zhang, X.; Yang, L.; Zhou, Y.; Wang, J. Experimental study of compressed air energy storage system with thermal energy storage. *Energy* **2016**, *103*, 182–191. [CrossRef]
36. Zaversky, F.; Fernández-Reche, J.; Casanova, M.; Monterreal, R.; Enrique, R.; Ávila-Marín, A.; Martínez, S.; Schmitz, M.; Castellanos, A.; Mallo, R.; et al. Experimental testing of a 300 kWth open volumetric air receiver (OVAR) coupled with a small-scale Brayton cycle. Operating experience and lessons learnt. *AIP Conf. Proc.* **2023**, *2815*, 100017.
37. Zaversky, F.; Rández, X.; Baigorri, J.; Sánchez, M.; Ávila-Marín, A.; Fernández-Reche, J.; Füssel, A. A Cost-Effective Open Volumetric Air Receiver Design Based on Free Floating Stackable Absorber Modules. In Proceedings of the SolarPACES 2022 28th International Conference on Concentrating Solar Power and Chemical Energy Systems, Albuquerque, NM, USA, 27–30 September 2022; Volume 1. [CrossRef]
38. Pabst, C.; Feckler, G.; Schmitz, S.; Smirnova, O.; Capuano, R.; Hirth, P.; Fend, T. Experimental performance of an advanced metal volumetric air receiver for Solar Towers. *Renew. Energy* **2017**, *106*, 91–98. [CrossRef]
39. Wu, Z.; Caliot, C.; Bai, F.; Flamant, G.; Wang, Z.; Zhang, J.; Tian, C. Experimental and numerical studies of the pressure drop in ceramic foams for volumetric solar receiver applications. *Appl. Energy* **2010**, *87*, 504–513. [CrossRef]
40. Luo, Y.; Zhang, Y.; Gao, Y.; Wang, X.; Xu, Z. Simulation and experimental study of high pressure switching expansion reduction considering real gas effect. *J. Cent. South Univ.* **2014**, *21*, 2253–2261. [CrossRef]

41. Jankowski, M.; Pałac, A.; Sornek, K.; Goryl, W.; Żołądek, M.; Homa, M.; Filipowicz, M. Status and Development Perspectives of the Compressed Air Energy Storage (CAES) Technologies—A Literature Review. *Energies* **2024**, *17*, 2064. [CrossRef]
42. KCE ThermoFluid Properties. *Property Library for Humid Air Calculated as Ideal Mixture of Real Fluids FluidDYM with LibHuAir for DYMOLA 2018*; KCE ThermoFluid Properties: Amberg, Germany, 2018.

https://doi.org/10.3390/app16136633